Integrated photoelectrochemical (PEC)-forward osmosis (FO) system for hydrogen production and fertigation application

Sifani Zavahir[1], Tasneem Elmakki[1], Mona Gulied[1], Ho Kyong Shon[2], Hyunwoong Park[3], Konstantinos E. Kakosimos[4], Dong Suk Han[1,5,*]

[1]*Center for Advanced Materials, Qatar University, PO Box 2713, Doha, Qatar*

[2]*Center for Technology in Water and Wastewater, School of Civil and Environmental Engineering, University of Technology Sydney, Sydney, NSW, 2007, Australia*

[3]*School of Energy Engineering, Kyungpook National University, Daegu 41566, Korea*

[4]*Chemical Engineering Program, Texas A&M University at Qatar, Doha, Qatar*

[5]*Department of Chemical Engineering, Qatar University, Doha, PO Box 2713, Qatar*

*Corresponding author

Dong Suk Han: dhan@qu.edu.qa

ABSTRACT

An integrated system with a photoelectrochemical (PEC) unit and forward osmosis (FO) in tandem operation was proposed in this study to combat water, energy, and food (WEF) deficiency. In an engineered approach, a combination of ammonium sulfite and ammonium sulfate solution was used to represent the wet flue gas desulfurization products of the ammonia scrubbing process commonly employed in oil and gas producing countries. In a continuous operating system, we showed that a sulfurous solution in the PEC process was oxidized under simulated sunlight to produce hydrogen, the ultimate clean energy, at a reduced titania nanotube array (TNA) working electrode (Energy). Then, the oxidized sulfurous solution entering the draw solution compartment of the FO unit was diluted when the system operated against simulated brackish water as the feed solution (Water). Recirculation of the draw solution effluent ensures continuous operation of the PEC and FO systems. Further application of this draw solution effluent as a cultivation solution to a basil plant at a certain time point showed visually favorable growth compared to the case supplied with tap water (Food). Therefore, this study stands out as the successful implementation of a bench-scale integrated system to simultaneously produce tangible outcomes for each of the deeply interlinked components of water, energy, and food.

Keywords: Forward osmosis (FO); Photoelectrochemical (PEC) system; Water-energy-food nexus; Hydrogen; Fertigation

1. Introduction

Food, water, shelter, and clothing were the basic human needs until the 1950s, after which automated mass production of electronics and computers began. As a result, energy has become a basic human need, so governments work at a strategic level to ensure that people have access to sufficient electrical energy/power to complete their daily tasks at the domestic level, despite the immense power consumption in industrial facilities. Coal and fuel combustion in power plants produce electricity and emits harmful SOx gas along with carbon and NOx emissions (flue gas) from fossil fuels [1]. The SOx concentration in the flue gas depends on the S content of the coal. According to Resnik *et* al., a pulverized coal-fired power plant using 2.8 % sulfur leaves 2000 ppm of SO_2 in the exhaust gas [2]. Depending on the throughput of the fuel, the sulfur gas in the fumes of a steam boiler can range from 4.4 $mg \cdot mol \cdot L^{-1}$ to 2 $mg \cdot mol \cdot L^{-1}$ [3]. This has led the government to stress the need to maintain stringent air quality standards to ensure the health and well-being of the surrounding environment, including the ocean. High levels of sulfur in the surrounding create acid rain and affect aquatic life. Therefore, the removal of sulfur from flue gases is intensely studied, and flue gas desulfurization (FGD) is an established field with regenerative and non-regenerative scrubbers used for SO_2 adsorption and removal [4]. The FGD systems appeared in the coal-fired power plant industry in the United States (US) and Japan in the early 1970s and then rapidly expanded in Europe in 1980 [5]. At present, wet limestone FGD, magnesium enhanced lime (MEL), and lime spray drying (LSD) have reached technology readiness (TR) level 9, and the efficiency has reached 90% SO_2 removal. Among them, LSD is less expensive to install but can only handle SO_2 removal in power plants operating up to 250 MW and burning low-to-medium sulfur coal [4].

In a relatively novel FGD with ammonia, SO_2 is absorbed in aqueous ammonia (NH_3) to form $(NH_4)_2SO_3$ or $(NH_4)_2SO_4$, as shown in the reactions below (R1-R2). It is preferred among other techniques due to the low parasitic load experienced in ammonia scrubbing [6]. The presence of trace contaminants such as F, As, B, Cl, Se, and Hg were captured by FGD without affecting sulfur removal [1]. The United States Environmental Protection Agency (USEPA) classifies ammonia FGD as non-regenerative because S is not separated from the scrubber after the absorption process [7]. Ammonia scrubbing flue gases under various experimental conditions with TR levels from 5-6 to 9 was tested. The ammonia scrubbing process at TR levels of 5-6 was demonstrated by the Powerspan Corporation company, a coal-fired power plant in Ohio, US that generates 50 MW [8]. If these wet FGD products from a non-regenerative ammonia scrubbing process could be exploited to find a solution to another basic human need, it would lead to net zero sulfur emission (R1-R3),

$$SO_2(g) + NH_3(g) + H_2O \xrightarrow{\text{chemical absorption}} (NH_4)_2SO_3(aq) \quad (R1)$$

$$(NH_4)_2SO_3(aq) + O_2 \xrightarrow{\text{air oxidation}} (NH_4)_2SO_4(aq) \quad (R2)$$

$$(NH_4)_2SO_3(aq) + H_2O \xrightarrow{\text{electrolysis}} (NH_4)_2SO_4(aq) + H_2 \quad (R3)$$

On the other hand, the need for self-sufficiency in access to water, energy, and food (WEF) is crucial to creating a safe society. The awareness of the undeniable interconnection between these three core resources has been very well understood over the past decade. It has been evidenced by a high number of research and discussions in academia and policy-making, strategic planning, and implementing frameworks to secure the trio with a holistic approach rather than looking at each component individually [9-14]. Most of the nexus studies were case studies of how countries or

regions have adopted new strategies and improved frameworks to ensure security for water, energy, and food [15-17].

The production, generation, purification and refining of water, food, and energy are done by appropriate and specific scientific and engineering approaches, and it is in the hands of policymakers and the governments to adopt specific technologies or implement the infrastructure. Therefore, it is imperative to keep the distinction between the two narrow. Much of the published work in this regard includes problem understanding and solution suggestions to conceptually address the elevated stress on WEF nexus resources [18]. However, this is not enough. Although our understanding of the interconnection of the WEF nexus has improved, only a little progress has been made in scientific research covering all elements of the nexus. There must also be a new way to leverage materials of non-commercial value and transform them into value-added content that ensures WEF sustainability [19].

The increasing pressure further supports the need for such a solution in the WEF nexus due to the deep interconnection between the expanding population and material consumption [14]. Veroneau et al. showed in one study that seawater concentrated with forward osmosis (FO) was fed to an electrochemical (EC) system to be used as an electrolyte for water splitting [20]. They affirmed that combining the two systems for the continuous operation of the EC system allows for the sustainable generation of oxygen- and hydrogen-based energy by water splitting.

In another study, Logan et al. highlighted the conceptual importance of hydrogen production using renewable energy sources and seawater electrolyzer [19]. In this regard, this study idealized a self-sustainable combined process that utilizes treated environmental pollutants ($(NH_4)_2SO_3$ and $(NH_4)_2SO_4$, produced in the FGD ammonia scrubbing process) as initial feed resources to produce the outcomes of water, food, and energy through specific processes with less

energy. Qatar, where the core research work is conducted, is a country with economic and related trade activities directly linked to the extraction and refining of natural gas. This process unavoidably releases sulfur-containing flue gasses into the atmosphere [21]. Our previous work demonstrated that ammonium sulfite and ammonium sulfate were suitably well used as a draw solution in fertilizer-drawn forward osmosis (FDFO) system [22]. In the salinity gradient-driven FO process, a high concentration of sulfur-based seed solution (SBSS) is used as a fertilizer draw solution (DS) and diluted to a low concentration by recovering water from brackish level water as a feed solution (FS). Findings revealed that DS with lower sulfite content leads to high desalination performance by providing high water flux and low reverse solute flux regardless of feed water type (DI water, seawater, or brackish water).

To meet the WEF needs, we further modified the FO system using the brackish water as FS and the SBSS stream derived from FGD as DS to operate in continuous flow as a system that can take on the pivotal dynamics of this study. Here, the FDFO system does not require the high pressure needed for desalination, such as RO, nor does the energy required to recover draw solutes from the mixed DS in a typical FO system [23-25]. The viable electron donor ability of SBSS can be used for hydrogen evolution by electrochemical (EC) water splitting. Embracing a suitable electrode capable of harvesting light will convert the EC process to photoelectrochemical (PEC), making the process more environmentally friendly [26, 27]. The diluted DS, rich in N and S, is attractive as a fertilizer and can be used directly in fertigation.

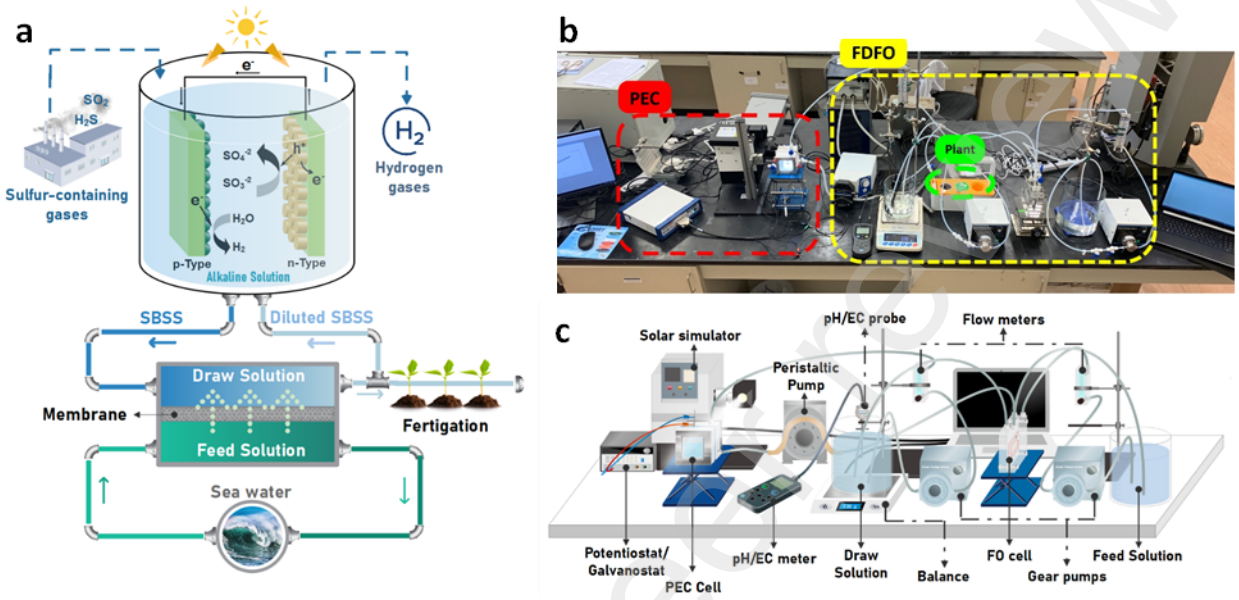

Fig. 1. From concept to experimental setup of an integrated water-energy-food (WEF) system. (a) Schematic representation of the solution for the water-energy-food nexus modeled in this study. (b) Photograph of a bench-scale PEC-FDFO setup. (c) Schematic diagram of a bench-scale PEC-FDFO hybrid system with performance evaluation devices such as salinity, pH meters, and scales.

Hence, this study demonstrated the synchronized operation of a bench-scale PEC-FDFO integrated system. The performance of the integrated system was monitored and maintained in terms of DS dilution level, salt rejection and the water recovery rate in the FO process (Water), and stability and photocurrent level of hydrogen evolution (Energy) in the PEC system, respectively. Meanwhile, the growth of basil plants (Food) fed with diluted DS was evaluated by visual observation with photographs taken at appropriate time intervals to highlight the utilization of the FGD products for reaching net zero sulfur emissions.

2. Materials and Methods

2.1. Chemicals

The chemicals used in the fabrication of the electrodes were phosphoric acid (H_3PO_4, 85.0%, Sigma-Aldrich), sodium fluoride (NaF, 99 %, Sigma-Aldrich), ethylene glycol $(CH_2OH)_2$, 99.5%, Scharlab), ethanol (C_2H_5OH, 99.7%, Scharlab), and acetone ($(CH_3)_2CO$, 99.80%, Scharlab). Feed and draw solutions (the PEC electrolyte) were prepared with ammonium sulfite solution ($(NH_4)_2SO_3$, 35% in H_2O, Sigma-Aldrich), ammonium sulfate ($(NH_4)_2SO_4$, 98.5%, Sigma-Aldrich), and sodium chloride (NaCl, 99.5%, Scharlab). All chemicals were of analytical grade and used directly as received. Both model feed and draw solutions were prepared by dissolving specific amounts of chemicals in deionized (DI) water.

2.2. Experimental setup of FDFO-PEC system

Fig. 1b and c present the bench-scale setup of the integrated system used in this study. The setup consists of two subsystems integrated; A PEC system that generates hydrogen gas using a sulfur-based seed solution (SBSS) as an electrolyte and a forward osmosis (FO) system that uses the SBSS circulated from the PEC system as the draw solution against the seawater feed solution to deliver an adequately diluted fertigation stream. The PEC system is a customized two-compartment cell (12 × 12 cm) using a three-electrode system configuration, one with a fabricated titania nanotube (TNA) electrode (working electrode) and the second with a Pt wire and saturated calomel electrode (SCE) as the counter and reference electrodes, respectively. A spacer and Nafion membrane (0.16 mm thick) separate the two compartments to hold the cell together and facilitate the transfer of protons throughout the experiment. Electrochemical data acquisition and analysis were performed via a potentiostat/galvanostat (Gamry, interface™ 1010). A SunLight™ solar simulator (ABET Tech., Inc.) was used to provide one sun intensity (AM 1.5 G, 100 $mW \cdot cm^{-2}$) to

drive photon-based electrochemical reactions. The FDFO system consists of a handmade FO test cell, two variable gear pumps (Cole-Parmer, USA), two flow meters (Cole-Parmer, USA), and tanks of feed and draw solutions. The FO cell has each symmetric channel on either side of the membrane, where water circulates from the feed solution (FS) side to the draw solution (DS) side in the closed loop. Instantaneous DS weight changes were recorded using a digital scale balance connected to the data logger software. This study used a commercial flat sheet thin-film composite (TFC) membrane (Toray Industries, Inc.) with an effective surface area of 36 cm^2 for FDFO tests. All tubes and fittings were 3/8" and 6" sizes, respectively. A peristaltic pump (Cole Palmer, Masterflex L/S) was used to facilitate the SBSS solution's passage from the PEC cell's outlet to the inlet on the DS side of the FO cell.

2.3. Electrode fabrication, characterization, and testing

A modified anodization technique was used to obtain highly ordered titania nanotube electrodes. In brief, small pieces of titanium (Ti) sheets (2 cm × 4 cm, 0.127-mm thick, 99.7% purity, Sigma-Aldrich) were cut and polished using sandpaper (400 grid) and polishing cloth to remove the oxidized layer on the surface and obtain a defect-free, flat surface for the subsequent steps. Next, Ti sheets were washed with acetone and ethanol for 10 minutes each in an ultrasonication bath (WiseClean, 40 kHz, 100 W) and then dried in a stream of nitrogen gas. The cleaned Ti electrodes were electrochemically anodized against a stainless-steel plate (3 cm × 5 cm) by applying a DC current of +30 V and 0.04 A for 4 hours. Electrochemical anodization was performed with dissolved H_3PO_4 (0.55 M) and NaF (0.14 M) in an aqueous electrolyte solution with a 4:1 ratio of deionized water to ethylene glycol. Continuous stirring of the solution was ensured throughout the anodization time to provide proper mass transport of the charged particles in the solution. Then, the as-obtained anodized electrodes were thoroughly washed using deionized

water and ethanol and then slowly dried in ambient air. To crystalize the synthesized TNAs, anodized TNA electrodes were annealed at 400 °C (annealed TNA) for 2 hours and then electrochemically reduced to black TiO_2 (reduced TNA) by applying a counter-current of -40 V against a Pt counter electrode in a phosphate buffer medium (0.1 M KH_2PO_4 buffer solution, pH 7.2) for 6 minutes.

The morphology of the fabricated electrode material and the active and support layer of the FDFO membrane was visualized by scanning electron microscopy equipped with energy dispersive X-ray spectroscopy (SEM/EDX, NOVANANOSEM 450, USA). The crystallographic structures of TNA electrodes fabricated at various fabrication steps were confirmed by X-ray diffraction (XRD, PANalytical Empyrean) in the 2θ angle range from 20^o to 70^o. Also, the surface roughness and depth of the fabricated electrodes were measured using a profilometer (Leica DMC 8 Profilometer). The functional groups of the active and support layers of the FDFO membrane material were characterized using Fourier transform infrared (FTIR-ATR, Spectrum 400 Perkin Elmer, USA) in the region of 4000 to 550 cm^{-1} with a scan rate of 32 scans. The surface energy of the FDFO membrane was calculated using the optical contact angles of water, ethylene glycol, and formamide on the FDFO membrane with the Owens, Wendt, Rabel, and Kaelble (OWRK) model. The contact angle device recorded surface contact angle measurements (OCA 35, DataPhysics, Germany). The thermal stability of the membrane material was evaluated by thermogravimetric analysis (TGA) performed at room temperature (RT) to 450 ^oC on TGA400 (Perkin Elmer, USA).

The electrochemical properties of the fabricated electrodes were characterized by cyclic voltammetry (CV), chronoamperometric and electrochemical impedance spectroscopy (EIS) tests. To assess the hydrogen evolution reaction on the electrode, CV (+1.2 V to -1.2 V vs. SCE) tests were performed at a scan rate of 50 $mV \cdot s^{-1}$. The solar simulator calibrated to 1 sun illumination

intensity (100 mW·cm^{-2}) was directed to the working electrode during 'light on' experiments, and the solar simulator was turned off for the dark experiment. The photoactivity and stability of the fabricated electrodes were evaluated by performing a chopped chronoamperometry at -0.25 V vs. SCE, along with EIS tests to assess the ohmic resistance at 100 kHz to 0.01 Hz frequency range. In addition, intermittent light chopping was done with the inbuild light shield in the solar simulator. All electrochemical performance tests were conducted using ammonium sulfate or/and ammonium sulfite-based single or binary electrolyte solutions, with initial solution concentrations (**Table 1**).

Table 1. Properties of fertilizer draw solution (FDS) at 1 M SBSS concentration, 25 °C, and 1 bar.

FDS	Molar concentration (M)		Conductivity (mS/cm)	Osmotic pressure (bar)*
	$(NH_4)_2SO_4$	$(NH_4)_2SO_3$		
DS1	1		99.3	31.12
DS2		1	92.6	28.03
DS3	0.8	0.2	96.1	30.43
DS4	0.6	0.4	97.5	29.78
DS5	0.4	0.6	93.6	29.16
DS6	0.2	0.8	91.9	28.58
DS7**	0.1	0.4	54.5	13.67

* Osmotic pressure estimated from AspenPlus software (Aspen ONE® version 9 software Aspen Technology. Inc.)
** DS concentration is 0.5 M, prepared to be half the molarity of DS 6

2.4. Evaluation of FDFO-PEC system

The integrated system experiments were first initiated on the PEC side. The PEC cell was initially stabilized by introducing deionized water as an electrolyte solution, performing a chronoamperometric test at -1.0 V for 3 minutes, and then conducting another similar chronoamperometric test with DS. Next, the PEC and FDFO systems were put into operation

simultaneously. At this stage, the PEC cell was filled with the test electrolyte solution, and the chronoamperometry scan was performed for 5 hours at -1.0 V with a scan rate of 50 $mV \cdot s^{-1}$. In each experiment, DS comes to the DS tank, passes through the PEC cell, and then enters the inlet of the FO cell.

Meanwhile, in the FDFO part of the system, all tests were carried out in FO mode, with the active layer of the FO membrane placed against the FS and the support layer facing the FDS. Initially, the FDFO system was stabilized using DI as FS and DS for 30 minutes. Several FDFO tests were then conducted by varying the flowrates of FS and DS solutions (0.5, 0.8, and 1 LPM) and the operating time (6 and 24 h). During the FDFO test, the temperature of FS and DS were maintained at room temperature (±25 °C) without mixing. In-situ hydraulic flushing was applied for 30 minutes after each FDFO run to reduce membrane fouling. The water quality of FS and DS was analyzed before and after each run using benchtop conductivity and pH meter (HQ portable meter, HACH, USA) and ion chromatography (850 Professional Metrohm, Switzerland). The performance of the FDFO process was evaluated in terms of water flux, specific salt flux, and percentage of salt rejection. The experimental water flux (J_w) was calculated by dividing the weight changes of DS (ΔW) (ΔW) over the operating time (Δt) and effective membrane area (A_{eff}), as expressed in Eq. (1).

$$J_w = \Delta W/(\rho A_{eff} \Delta t) \qquad \text{(Eq. 1)}$$

The reverse solute flux (J_s) of the individual component of DS (NH_4^+, SO_4^{2-}, and SO_3^{2-}) that diffuses back to the feed side due to the concentration gradient between DS and FS can be determined as expressed in Eq. (2).

$$J_s = \frac{(V_i - V_P)C_r}{A_{eff}\, t} \qquad \text{(Eq. 2)}$$

where V_i and V_p are the initial volumes of FS and the permeate volume of pure water from FS to DS, C_r is the concentration of draw solutes in the feed side at the end of the experiment, and t is the operating time of the experiment.

The percentage of salt rejection (R%) of ions of FS (Na^+, Cl^-) that may diffuse through the FO membrane from the feed side to the draw side is expressed in Eq. (3).

$$R\% = \frac{C_{F_i} - \frac{C_{D_f}(V_i - V_P)}{V_P}}{C_{F_i}} \quad \text{(Eq. 3)}$$

where, C_{F_i} and C_{D_f} are the initial and final concentrations of ions in FS and DS, respectively.

2.5. Draw and feed solution preparation

Ammonium sulfate ($(NH_4)_2SO_4$) and ammonium sulfite ($(NH_4)_2SO_3$) were used as draw solution (DS). Two different concentration categories were studied. The initial study was performed on diluted concentrations where FS was 3 g/L NaCl and DS ranged appropriately from 0.16 M to 0.36 M $(NH_4)_2SO_4$ solution as the single component FDS. Binary mixtures of $(NH_4)_2SO_4$ and $(NH_4)_2SO_3$ with a total salt concentration of 0.24 M coupled with 3 g/L NaCl FS were employed before using high concentrations. DS. and FS in the upscaled PEC-FDFO system. FS was 5 $g \cdot L^{-1}$ NaCl, whereas DS had a total salt concentration of 1 M prepared with $(NH_4)_2SO_4$ or $(NH_4)_2SO_3$ in DI. Detailed characteristics of 1 M DS are given in **Table 1**.

3. Results

3.1. Characterization of TNA electrode

During PEC operation, sulfur-based seed solutions (SBSS) prepared with ammonium sulfate and/or ammonium sulfite in aqueous media first enter the PEC cell. SBSS is the catholyte electrolyte and produces hydrogen gas by water electrolysis in the PEC device with reduced titania nanotube arrays cathode upon solar light illumination. Morphology of the reduced TNA is tubular arrays of a high order as affirmed by FE-SEM given in **Fig. 2a**. TNAs grown on Ti film by anodization technique offer two advantages. One is a film electrode that facilitates unprecedented use in commercial-scale applications [28, 29]. Second, the titania phase self-supported on the Ti substrate provides better stability and adhesion between the electroactive film and the substrate [30, 31]. A well-defined long-range order of hollow-centered arrays in the reduced TNA is the retention of the arrangement from the anodization step to the annealing and reduction process (**Fig. S1**). The XRD analysis of the annealed TNA film showed sharp peaks at 25.30^{o}, 38.57^{o}, and 48.02^{o}, corresponding to the presence of (101), (004), and (200) planes confirming the crystallization of the anatase phase during annealing (**Fig. 2b**). Jeong and coworker made similar observations when they fabricated TNA in an anodization mixture consisting of 2% of DI water in ethylene glycol electrolyte [30]. XRD clearly shows the anatase phase formation during annealing and the presence of the phase through the reduction process. Anatase phase titania is the most studied semiconductor material for various applications utilizing UV light [32, 33]. Creating oxygen vacancies by reducing some of the Ti^{4+} sites in the titania shifts the band edge slightly towards the visible region. The photoluminescence (PL) spectra recorded for the annealed and

reduced electrodes upon excitation at 375 nm showed a higher PL intensity for the annealed electrode, but the intensity decreased significantly for the reduced electrode (**Fig. 2c**). Since the PL intensity is related to the electron-hole recombination rate, the charge recombination rate of the reduced TNA was observed to be significantly lower than that of the annealed TNA, facilitating a higher rate of light-induced activity. In addition, the band structure calculated from the PL spectra revealed the reduced TNA to have a bandgap of 2.75 eV. Surface topography analysis shows a relatively smooth surface on the reduced TNA electrode with a surface roughness parameter of 0.5536 µm, as depicted in **Fig. 2d,** but higher with 0.6376 µm (**Fig. S2**) when annealed, indirectly confirming that the reduction process was successful.

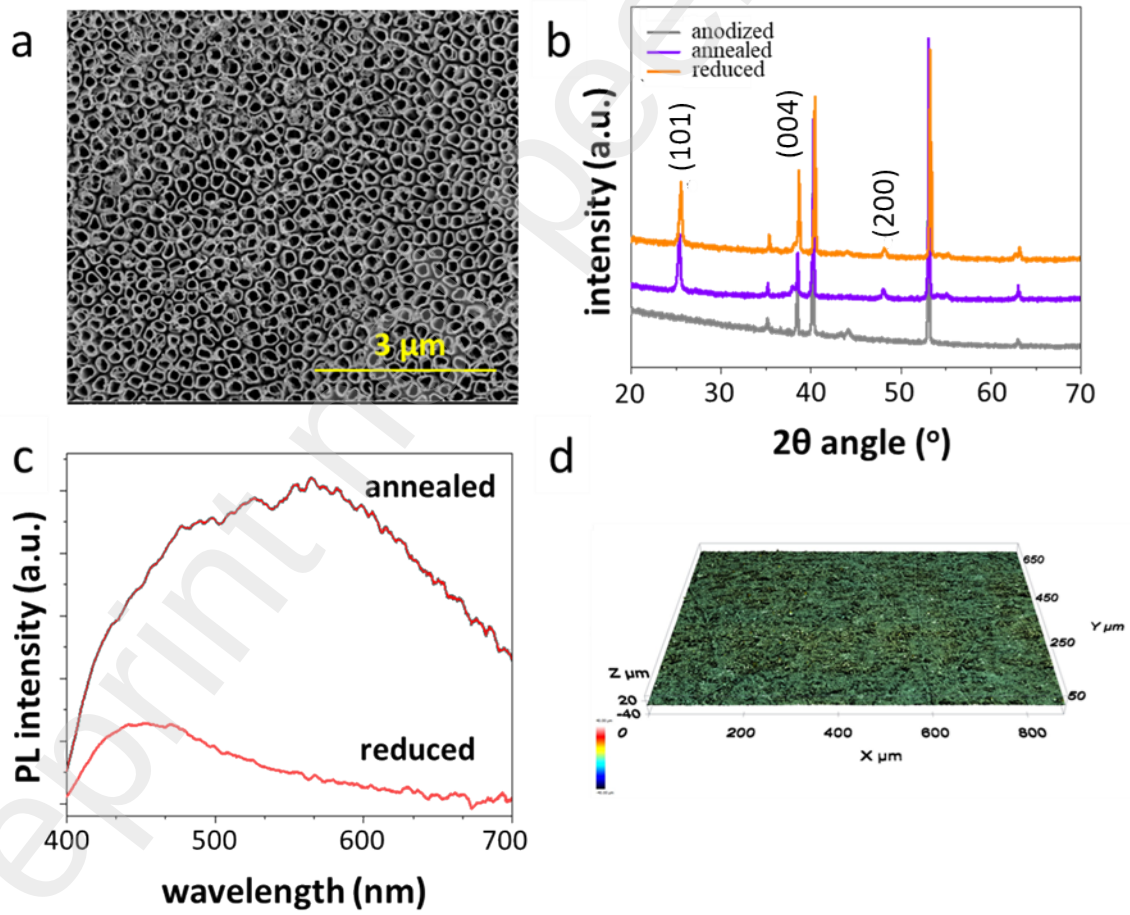

Fig. 2. The surface analysis of titania nanotube array (TNA) electrodes. (a) SEM image of reduced TNA electrode. (b) XRD data were collected in the 2θ angle range from 20° to 70° (anatase diffraction angles indexed). (c) PL intensity in the 400 – 700 nm range upon excitation at 375 nm. (d) Surface topography of reduced TNA electrode captured by a profilometer.

3.2. Photoelectrochemical (PEC) performance

As reduced TNA is the cathode electrode of PEC in the integrated process, the light-induced electrochemical behavior of the reduced TNA was evaluated in a singular $(NH_4)_2SO_4$ electrolyte in a stand-alone process operation, and its performance was compared with its anodized and annealed counterparts. Cyclic voltammetry (CV) tests performed in 0.1 M $(NH_4)_2SO_4$ electrolyte solution to study the initial hydrogen evolution revealed that TNA electrodes fabricated in the study are capable of producing hydrogen gas (**Fig. 3a**) intensively upon light illumination conditions. The onset potential, an important parameter for evaluating the relative hardness when producing hydrogen gas, showed a favorable trend. According to the values derived from the CV curves given in **Fig. 3a,** the onset potential values were -0.36 V, -0.12 V, and -0.06 V for anodized, annealed, and reduced TNA, respectively. The reduced TNA electrode showed a high current density of ~ -7 $mA \cdot cm^{-2}$ at -0.6 V (vs. SCE). This value is significantly higher than the previous observation made with 0.1 M Na_2SO_4 electrolyte and TNA material on FTO glass [30], where the maximum current density was only -0.1 $mA \cdot cm^{-2}$. In the latter case, the scan rate was 5 $mV \cdot s^{-1}$, whereas it was maintained at 50 $mV \cdot s^{-1}$ in the present study. The scan rate affects the limited diffusion current when the entire reaction or part of a reaction is diffusion-controlled. Therefore, higher current densities are expected at higher scan rates. Chronoamperometry was used to evaluate electrochemical reactions' stability and progression by examining the current density at an applied potential value known to be electrochemically active. The chopped chronoamperometric test, typically performed on PEC systems, provides additional information about the photo-induced chemical reactions, producing crest and trough for light on and off

regions, respectively (**Fig. 3b)**. Chopped chronoamperometric test at -0.25 V (vs. SCE) exhibited a sound increase in light-induced photoactivity of reduced TNA compared to annealed. The anodized electrode did not show activity regardless of the on or off of light, which is expected because the applied potential (-0.25 V) is less than the onset potential of the anodized TNA (- 0.36 V) electrode. The stable and constant photocurrent plateau in the chopped chronoamperometric curve's light on and off regions affirms sufficient band bending in the TNA material, alleviating local charge recombination. Hence, these observations strongly suggest that reduced TNA has a more significant potential to be a cathode for HER in the integrated process. EIS analysis provides insight into the resistive layer thickness between the electrode and the electrolyte. **Fig. 3c** exhibits a wider resistive barrier for the anodized electrode primarily related to its surface roughness because there was no annealing. A much narrower resistive barrier to the reduced TNA electrode was seen, which is directly related to improved HER rates of the reduced TNA. The EIS analysis was further studied using reduced TNA electrodes under the same experimental conditions except for keeping the system dark. The resistive barrier in the dark was more significant than that of the light (**Fig. 3d**), which confirmed the formation of a higher conductive layer when the light was induced, resulting in more enhanced HER performance of the reduced TNA electrode. In another study, Jeong and coworkers justified that the lower resistive layer of the reduced TNA was due to the reduced charge transfer resistance occurring at Ti^{3+} and oxygen vacancies sites compared to only annealed electrodes [27].

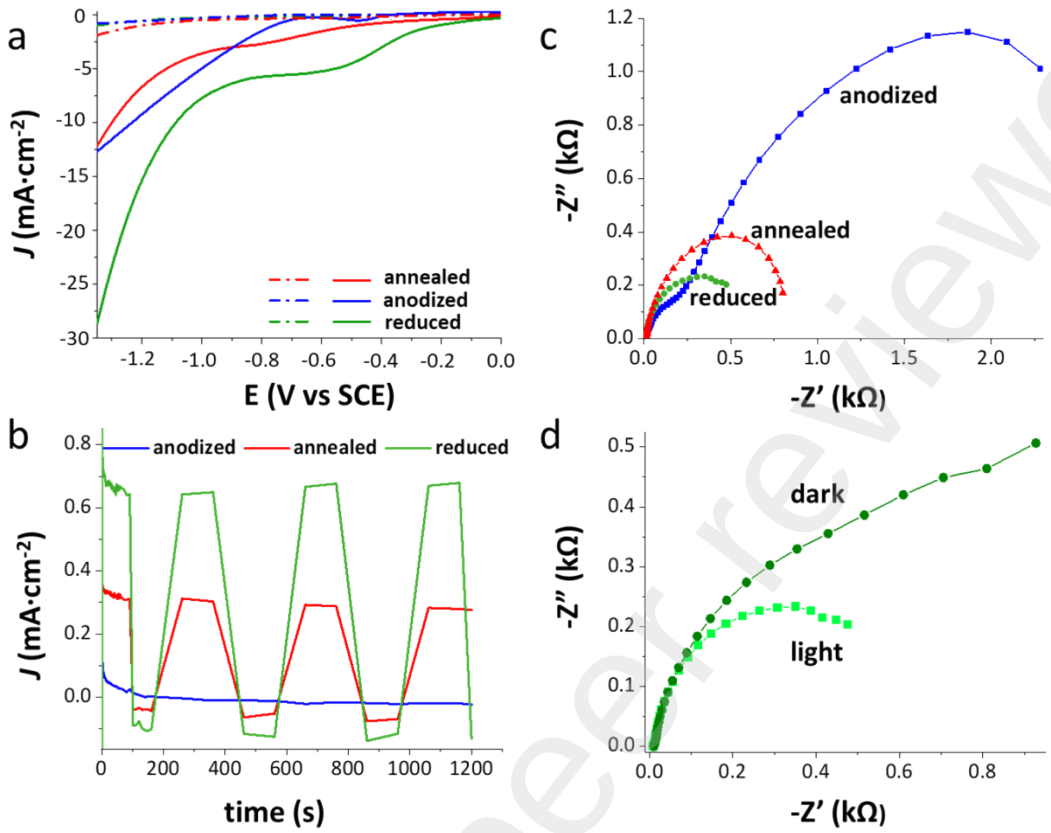

Fig. 3. Photoelectrochemical characterization of the fabricated TNA electrodes. (a) CV curves; The solid line represents the 'light on' experiment, and the dashed line refers to the 'light off' condition for the same experiment. (b) Chopped chronoamperometry. (c) EIS was measured in light for anodized, annealed, and reduced TNA electrodes. (d) Comparison of EIS responses of reduced TNA electrode under light and dark conditions in 0.1 M $(NH_4)_2SO_4$ electrolyte within the frequency range of 100 kHz to 0.01 Hz.

3.3. Fertilizer-drawn forward osmosis (FDFO) performance

The FDFO system operated with a flat sheet commercial thin-film composite (TFC) FO membrane and two solution streams, where DS was SBSS similar to catholyte used in the PEC process and FS was brackish level water (3 g/L NaCl). To ensure sufficient osmotic energy to facilitate the FO run, DS (0.16 M $(NH_4)_2SO_4$) was maintained at a concentration three-fold higher than FS. FO runs were performed in the FO mode, where an active layer (AL) of the FO membrane

faced the feed side while the support layer (SL) faced the draw side. SEM indicated very fine and periodic surface features similar to feathers on the 5 μm scale in the AL (**Fig. S3a)**, and the SL showed surface pores of 30 μm length and 70 μm width with a long-range periodicity at intervals of ~100 μm (**Fig. S3b**). Despite the morphology difference in the two sides, FTIR analysis of AL and SL showed a similar peak pattern except for the two minor peaks on the AL side located at 1732 and 1540 cm^{-1}, corresponding to the COO- and C=O functional group, respectively (**Fig. S4**). Membranes were highly thermally stable (<1% weight loss) up to 150 ^{o}C, with a weight loss of <3% until 380 ^{o}C based on the TGA curve (**Fig. S5)**. This allows the membrane to withstand local temperature fluctuations without compromising membrane integrity. The surface wettability and ability of the membrane to compensate for fluid influx and outflux is one of the essential features governing FO performance. Knowing the surface energy of a membrane can provide insight into surface exposure and bulk interactions. Hence, the surface energy was calculated using the contact angles of the membrane in different solvents using the Owens, Wendt, Rabel, and Kaelble (OWRK) model. The contact angles of AL in the fresh membrane were 60±1.2^{o}, 36±1.6^{o}, and 0 in DI water, ethylene glycol, and formamide, respectively, and the surface energy was calculated to be 48.6 $mJ \cdot m^{-2}$. The same range of surface energy was observed in another study using homemade poly(ethylene glycol) phenyl ether acrylate (PPEA) active layer. The authors found that the surface energy (42.95 $mJ \cdot m^{-2}$) of pure PPEA decreased to 40.37 $mJ \cdot m^{-2}$ when 25% of the PPEA was replaced with methacrylic acid (MAA) to make the 75:25 (w/w %) ratio of PPEA to MAA copolymer system [34]. Moreover, this positive surface energy value could retard the interaction between the foulant and the membrane surface, reducing ion concentration polarization (ICP) and preventing the decrease in water flux from the FS side to the DS side [35].

The FDFO system performance was evaluated at different operating flow rates of 0.5, 0.8, and 1.0 LPM (**Fig. S6**). Both FS and DS were maintained at the same flowrate. As a result, the water flux and % water recovery increase with increasing flow rate. At 0.5 LPM, water flux was 27.0 LMH with 2.45% of water recovery. Increasing the flow rate to 0.8 LPM enhanced the flux to 28.3 LMH, and at 1.0 LPM, the recovery increased to 2.55%, resulting in a greater flux and recovery increase compared to those obtained from 0.5 to 0.8 LPM flowrate increments. The pumping flowrate indirectly and inversely represents the residence time of the inflow into the FO chamber, and an increase in the pumping flowrate indicates a decrease in the interaction time with the FO membrane. In addition to water flux and recovery, the flowrate significantly impacts the solution quality in DS concerning salt rejection and reverse solute flux. At 1.0 LPM, 31.8 LMH flux and 2.86% water recovery were observed with a good salt rejection of 99.3%. The salt rejection at 1.0 LPM was in the same range as those at 0.5 LPM (99.4%) and 0.8 LPM (99.3%). Hence, further experiments involving the integrated PEC-FDFO system were set to 1.0 LPM as the working flowrate.

3.4. Integrated PEC-FDFO system for fertigation

The previously described individual FDFO and PEC systems were combined in a tandem manner. In operation, SBSS enters the PEC system first and undergoes hydrogen evolution, and then the outlet stream of the PEC enters the DS side of the FO system. The integration modified the flow path in the DS of the FO system and streamlined it with an extra peristaltic pump, as shown in **Fig. 1**.

The initial evaluation of the integrated system was performed with a single component $(NH_4)_2SO_4$ DS. The FDFO desalination performance as a function of DS concentration was monitored for an integrated system operating for 2 h at 1.0 LPM with a constant FS concentration

of 3 g/L NaCl. Test runs were performed with four different $(NH_4)_2SO_4$ DS concentrations (i.e., 0.16, 0.20, 0.24, and 0.36 M). The results show that water flux and % water recovery increased with increasing DS concentration from 0.16 M to 0.24 M $(NH_4)_2SO_4$, while water flux was lower than expected for 0.36 M $(NH_4)_2SO_4$ at 23 LMH water flux (**Fig. S7**). In contrast, 0.24 M $(NH_4)_2SO_4$ produced a higher flux of 32 LMH. While the osmotic gradient visualized by DS and FS concertation difference is the main driving force for higher flux, concentration polarization (CP) might have a detrimental impact on water flux. Within the porous layer of the asymmetric membrane (**Fig. S3**), a virtual boundary layer stands as a guard protecting the membrane from turbulence and shear force. This internal concentration polarization decreases the effective osmotic driving force between the two (FS and DS), so it is reasonable to experience a lower water flux at 0.36 M $(NH_4)_2SO_4$.

Moving on to the practical purpose of integrating the PEC and FDFO processes, the electrolyte and DS solution used in the integrated system was prepared as single and binary mixtures of $(NH_4)_2SO_4$ and $(NH_4)_2SO_3$ SBSS with a total concentration of 0.24 M. Binary solutions were prepared with three different salt ratios (i.e., 3:2, 1:1, 2:3) of $(NH_4)_2SO_4$:$(NH_4)_2SO_3$. Similar to previous FDFO runs, FO was evaluated in terms of water flux and water recovery, and PEC performance was assessed by a CV (**Fig. 4**). One CV test was carried out 10 minutes after the start of the test to ensure that the system was stable and running, and another test was performed at the end of the 2-hour operation of the integrated PEC-FO system. As a Pt-free HER catalyst, the reduced TNA electrode performed well with a cathodic current oscillating around -20 $mA \cdot cm^{-2}$ at an electrode potential of -1.0 V (vs. SCE). Additionally, the cathodic current change at -1.0 V (vs. SCE) after 2 h was less than 4% of the initial value, confirming the suitability of the sulfur-based binary electrolyte for hydrogen gas generation.

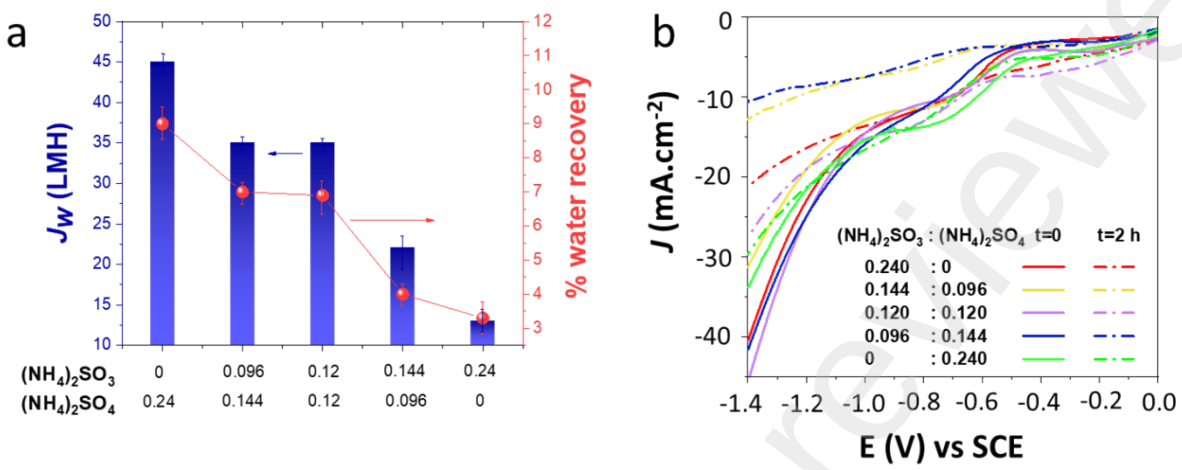

Fig. 4. Performance of an integrated PEC-FDFO system at FS concentration of 3 g/L NaCl, flowrate of 1 LPM, and run time of 2 hours. (a) Water flux and % water recovery vs. various ratios of DS component concentrations at a total DS concentration of 1M. (b) Corresponding CV curves representing current density (*J*) vs. potential (*E* vs. SCE) measured in the PEC part of the integrated system operation.

Some trends in current density were seen based on the sulfite to sulfate ratio in the starting electrolyte. At potentials higher than -1.0 V (vs. SCE), the current density tended to increase with increasing sulfite content until the sulfite to sulfate ratio was 1:1, i.e., the order of the current densities of ($(NH_4)_2SO_4$:$(NH_4)_2SO_3$) is (1:0) < (3:2) < (1:1). The lowest current density was observed in the 2:3 ($(NH_4)_2SO_4$:$(NH_4)_2SO_3$) system (**Fig. S8**). The current density after 2 h of PEC-FDFO run initially showed a drop in cathodic current but is high enough (minimum -10 mA·cm^{-2}) to ensure the operability of the integrated process even at high dilution levels. Conversely, the change in current density after 2 h of PEC-FDFO operation at -1.0 V (vs. SCE) was insignificant at -1.0 V for all single and binary combinations. Regardless of the measured potential, the ammonium sulfite alone system maintained a higher current density, and the ammonium sulfate alone system maintained a constant current density during the 2 h PEC-FDFO

run. This is because hydrogen evolution occurs in the complementary reduction process as a result of potential sulfite-to-sulfate oxidation. Water flux showed an increasing trend with increased ammonium sulfate concentration in the ammonium sulfite: ammonium sulfate binary solutions ranging from 13 LMH for 0.24 M $(NH_4)_2SO_3$ solution to 45 LMH with 0.24 M $(NH_4)_2SO_4$. % Water recovery in this scenario, where the operation was conducted for 2 hours only, followed a similar pattern to that of water flux (**Fig. 4a**).

Finally, the system upgraded the total SBSS salt concentration of DS to 1 M. The integrated process's water flux and water recoveries were in a similar range (**Fig. 5a**) and comparable to a single FDFO system previously studied by our research team [22]. Despite continuous dilution, the PEC was maintained at a constant potential of -1.0 V (vs. SCE) until the integrated system to collect a large amount of hydrogen gas was completed. In all cases except for 0.6:0.4 or 0.4:0.6, hydrogen evolution measured at -1.0 V for 5 hours (18000 s) (**Fig. 5b**) gives a stable current and gradually increases the cathodic current until equilibrium is reached. Interestingly, when the sulfite: sulfate ratio is closer to 1:1 (either 0.6:0.4 or 0.4:0.6), the gradual change in the respective chronoamperometric current over time was minimal compared to other solution compositions. Among binary mixtures, the most stable cathodic current density of 0.15 $A \cdot cm^{-2}$ was observed in the solution where the concentration of $(NH_4)_2SO_3$ (0.8 M) was higher than that of the $(NH_4)_2SO_4$ (0.2 M). It is interesting to see that the hydrogen evolution performance in the present integrated process is comparable with TNA under sodium sulfite (Na_2SO_3) and sodium sulfide (NaS_2) binary electrolyte with a total salt concentration of 1 M under light irradiation (100 W/m^2, AM 1.5G) [26]. During the integrated PEC-FDFO operation, the ammonium sulfate electrolyte system is slightly acidic (pH 5-6), whereas the binary solution and ammonium sulfite are near the neutral pH range (pH 7-8). In these scenarios, hydrogen evolution is most likely driven by an initial water

dissociation step (R4), generating (H adsorbate) H_{ads} at the surface adsorption sites on the electrode, which is regarded as '*E*', followed by the recombination of H_{ads} to give rise to hydrogen (R5-R6).

$$E + H_2O + e^- \leftrightarrow EH_{ads} + OH^- \quad \text{(R4)}$$

$$EH_{ads} + H_2O + e^- \leftrightarrow E + H_2 + OH^- \quad \text{(R5)}$$

$$2EH_{ads} \leftrightarrow 2E + H_2 \quad \text{(R6)}$$

Long tubular titania nanoarrays in the cathode electrode provide an improved solid-solution interface promoting the radial transfer of minority charge carriers into the solution. This vector charge transfer results in an elevated reaction rate when light absorption by the electrode is optimal [26].

Detailed evaluation of the DS and FS solution compositions after 5 hours of PEC-FDFO operation revealed that the 0.8:0.2 ratio of $(NH_4)_2SO_3$:$(NH_4)_2SO_4$ had the highest salt rejection among binary mixtures, as given in **Fig. 5c**. Therefore, the best-case scenario is to have the highest salt rejection and the least reverse solute flux (RSF). However, the RSF was higher at 0.8:0.2 $(NH_4)_2SO_3$:$(NH_4)_2SO_4$ than other binary solution combinations (**Fig. 5d**). As the pH in sulfurous electrolytes increases, the SRSF increases, and the water flux decreases. Consistently, higher ammonium sulfite content in the above case led to pH 7.65 compared to pH 5.31 for 1 M ammonium sulfate. The RSF was 6.8 gMH for SO_3^{2-} and 4.2 gMH for NH_4^+, respectively. Johnson et al. justified such behavior that if there were a large osmotic pressure gradient between FS and DS across the FO membrane, the DS would be further diluted until the osmotic pressure difference reached equilibrium [36]. Having as little salt as possible in the diluted DS to not exceed a conductivity level of 2 $mS \cdot cm^{-1}$ is important for direct use in fertigation, but it should also be accompanied by consideration of the trade-offs between water flux and dilution rate. Theoretically,

the salinity of DS would be expected to improve water flux and recovery rate by increasing the osmotic pressure differential, but experimental results show that water flux from the FS to the DS becomes lower over time at high DS. This is due to the unavoidable effects of dilutive internal concertation polarization (DICP) and RSF. DICP becomes dominant when more dilution occurs within the SL of the FO membrane that faces the DS side, which reduces the osmotic pressure of the DS and lowers the effective osmotic pressure gradient across the FO membrane [37]. On the other hand, RSF becomes significant at high DS concentrations as it induces DS solute diffusion across the membrane toward the FS side [38]. Therefore, according to the water flux and water quality data along with chronoamperometric data, the 0.8:0.2 ratio of $(NH_4)_2SO_3$:$(NH_4)_2SO_4$ is the most appropriate solute ratio with optimal water desalination and energy harvesting property.

Based on the salinity values, the highest % dilution was observed for DS using 0.4 M $(NH_4)_2SO_3$ and 0.6 M $(NH_4)_2SO_4$. However, the PEC system shows a higher cathodic current with increasing sulfite content. As sulfite was converted to sulfate in the coupling anodic process during the HER at the working electrode, the sulfite content conversely facilitated and affected HER, as shown in **Fig. 5b**. Continuous dilution of the integrated system gradually changes the salt concentration of the DS. Hence, considering a sequential 50% dilution level, system operability was assessed with two different salt concentrations (0.5 M and 0.25 M) while maintaining the same ratio (4:1) between ammonium sulfite and ammonium sulfate.

Although a fixed 4:1 ratio of $(NH_4)_2SO_3$:$(NH_4)_2SO_4$ was applied to the FO, the water flux and % water recovery tended to decrease proportionally as the total salt concentration of the DS decreased (**Fig. 5e**). The trend of chronoamperometric performance at -1.0 V was not different from that of water flux. In all three systems, the cathodic current densities were initially stable for a short time and then continued to increase until a final equilibrium was reached (**Fig. 5f**) due to

the simultaneous electrochemical involvement of ammonium sulfite. Here, the 0.4:0.1 ratio case had the highest cathodic current density (0.1 $A \cdot cm^2$) at equilibrium compared to other cases. However, the salinity of DS decreased more rapidly in the case of 1 M (0.8:0.2) than in other cases because the degree of dilution (% water recovery) is expected to be the highest at a high total DS concentration. Apparently, long-term FDFO operation with a high concentration of DS shows improved water recovery compared to starting with a low concentration of DS when the FS is constant. Hence, an FDFO system operating for 6 hours in integrated mode was extended an additional 18 hours in the standalone FDFO mode for a total operating time of 24 hours.

In the long-term FDFO operation, water flux dropped as expected from 6 to 24 h, yet % water recovery in the DS side increased remarkably (more than doubled) with the % dilution, as shown in **Fig. 6a**. Also, **Fig. 6b** shows that the solution resulting from the 24 h operation of the FO with the 0.8:0.2 ratio has a conductivity much closer to the initial conductivity of the 0.4:0.1 ratio solutions. Dilutions greater than 40% from the initial concentration are promising and prompt further studies.

In addition to process integration and good performances, the FO membrane and the reduced TNA electrodes must be stable through multiple integrated cycles. In this regard, the morphology of AL in the FO membrane was tested by SEM after 10 cycles of PEC-FDFO operation in 0.2 M $(NH_4)_2SO_4$ and 0.8 M $(NH_4)_2SO_3$ DS. The surface features of AL at the 5 μm scale showed no appreciable scale formation or rupture (**Fig. S9a)**. Also, the surface energy test performed on the dried membrane produced a surface energy of 47.71 $mJ \cdot m^{-2}$, a negligible reduction in the surface energy of the fresh membrane (48.59 $mJ \cdot cm^{-2}$). Similarly, the reduced TNA electrode visualized by SEM showed no significant changes in the tubular structure or

surface agglomeration, confirming the recyclability of the FO membrane and the reduced TNA electrode in the PEC-FDFO system (**Fig. S9b**).

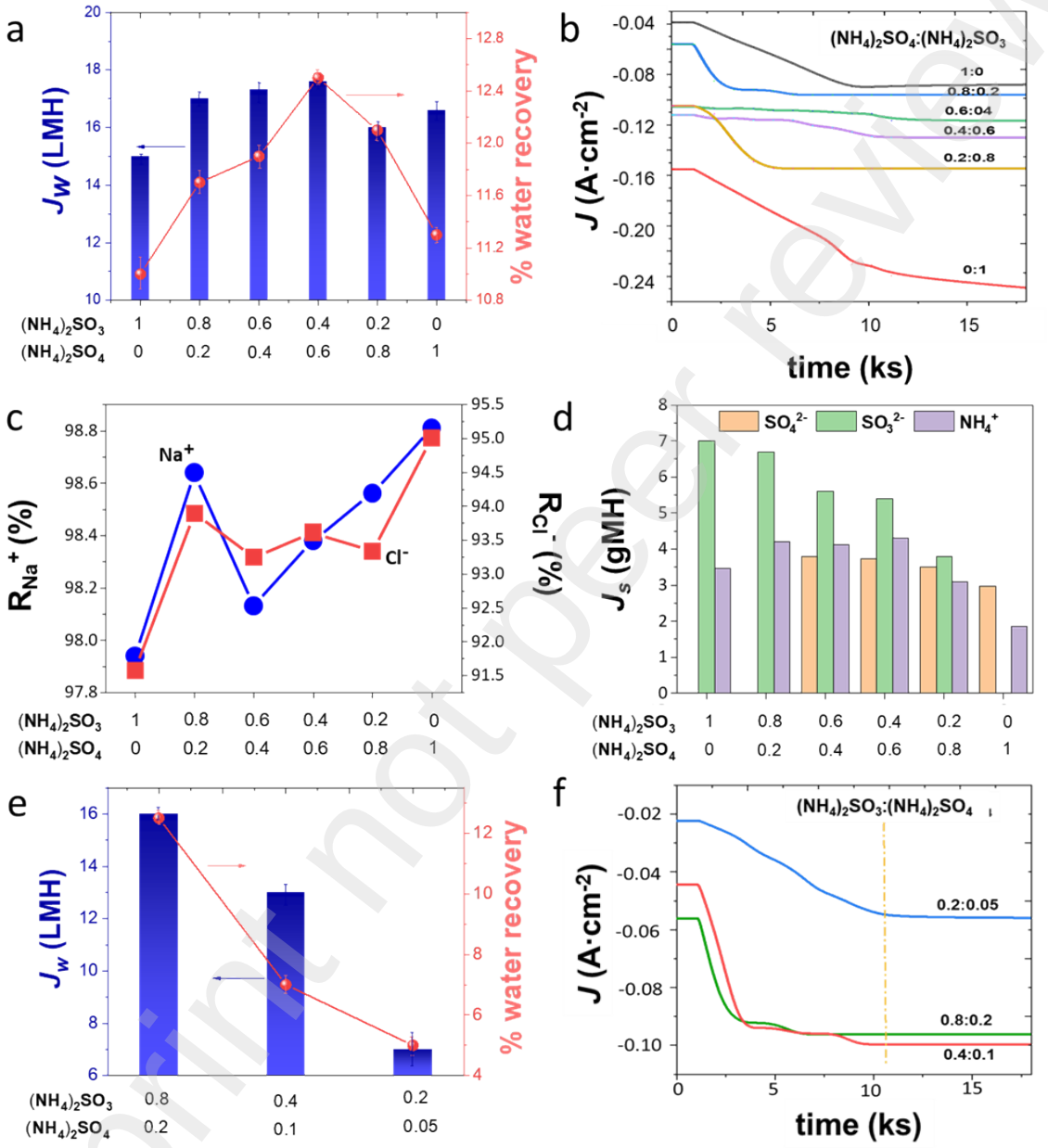

Fig. 5. Performance of integrated PEC-FDFO system at an FS concentration of 5 g·L^{-1} NaCl, a total DS concentration of 1M with different DS component concentration ratios, and a flow rate of 1 LPM. (a) Water flux (J_w) and % water recovery vs. various ratios of DS component concentrations. (b) Corresponding chronoamperometric curve measured at -1.0 V (vs. SCE) vs. current density (J). (c) Individual Na^+ and Cl^- salt rejection (R%) vs. various ratios of DS

component concentrations. (d) Reverse solute flux (J_s) vs. different ratios of DS component concentrations. (e) Water flux (J_w) and % water recovery vs. various ratios of DS component concentrations at a constant 4:1 molar ratio of $(NH_4)_2SO_3$:$(NH_4)_2SO_4$. (f) Corresponding current density (J) vs. time measured in the PEC system at -1.0 V (vs. SCE).

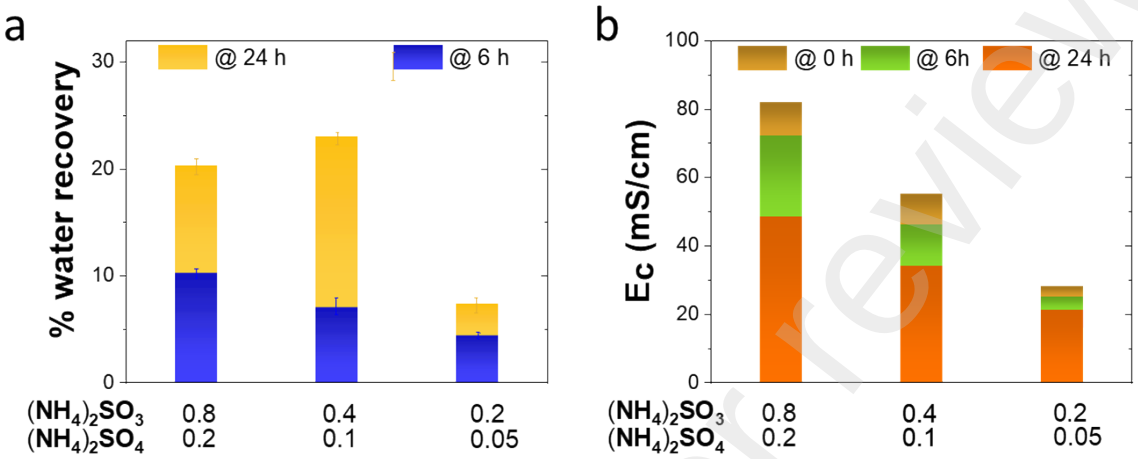

Fig. 6. Evaluation of FDFO process in an integrated PEC-FDFO system after 6 and 24 hours of operation. (a) Variation of % water recovery vs. various ratios of DS component concentrations. (b) Comparison of conductivity drop vs. various ratios of DS component concentrations.

3.5. Evaluation of fertigation performance by basil plant growth

Plant growth was assessed by growing two basil pants side by side, one fed with municipal water and the other fed with a diluted solution in a DS reservoir after the integrated system was run. To clearly understand shoot growth, leaf number and stem height were plotted against the number of days (**Fig. S10**). It exhibits that the plant fed with DS from day 9 showed outstanding growth in terms of leaf number and plant stem height compared to the other plants fed with municipal water. Leaf counts were always more than twice as high in DS-fed plants as in municipal plants. In addition to the number of leaves, the leaves reach maturity over time and grow into larger ones. The development of plant stem height indicated a higher rate in the DS-fed plant, but the height increment was linear up to 45 days, after which there was a shift in exponential height change.

This may be related to the faster growth of stem-derived branches (stem height in **Fig. S10b** is the cumulative height of the stem and branches). As discussed, this result strongly supports the additional advantage of utilizing sulfur-containing electrolytes in fertigation over municipal water regarding leaf density. Compared to the photos given in **Fig. 7 and Fig. S11**, this massive growth may be due to the presence of sulfur in the DS. NPK elements (nitrogen, phosphorous, and potassium) are the primary nutrients required by any plant. Next to those, sulfur plays a crucial role in producing chlorophyll and metabolizing nitrogen [39]. This study stands out as a visual indication of the contribution of sulfur to plant growth.

Fig. 7. Evaluation of basil plant growth with diluted draw solutions compared to the control over time (day). Plants with the label ‘s’ were fed the diluted draw solution.

4. Conclusion

In response to the needs for self-sustainable water, energy, and food nexus, this study successfully demonstrated the use of FGD-products-derived SBSS to produce substantial hydrogen photocurrents at a reduced TNA cathode in a light-induced electrochemical process while simultaneously oxidizing SBSS in a complementary anode. The effluent of SBSS oxidized in the PEC process is directed to the FO process as DS, where brackish water (5 g/L) was used as FS to allow water flux towards the DS side by an osmotic pressure gradient, resulting in significant dilution of DS that could be used in the fertigation process. The DS prepared with 0.8 M $(NH_4)_2SO_3$ and 0.2 M $(NH_4)_2SO_4$ was found to provide the most stable chronoamperometric current of 0.15 A cm^{-2} at -1.0 V (vs. SCE) with a dilution of 20% and 43% after 6 h (integrated) and 24 h (individual) system operation, respectively. The usefulness of the diluted DS for plant growth was confirmed by comparative monitoring of basil plant growth in a control group fed with plain water. Leaf density and stem height growth comparison of the two plants stand out as clear evidence of the contribution of sulfur to plant growth. The operation of PEC-FDFO has many benefits compared to the individual operation. One of the key benefits is that the DS coming after the PEC process undoubtedly is rich in hydrogen gas. Recently the role of hydrogen-rich water in plant growth and its anti-oxidant properties have been under immense study [40, 41], and the observed tremendous growth of the plant can be ascribed to the aforementioned hydrogen-rich water and other nutrients. The combined process also facilitates the use of high sulfite concentrations in FDFO. Further, the adhesion, stability, and durability of reduced TNA film electrodes are very high, and this can be commercialized. A slight improvement in the counter electrode to replace Pt with a cost-effective alternative will facilitate the small test units of this integrated system to be used in agricultural lands where energy is highly scarce. Through this vision, this study can contribute significantly to the WEF field as it is the first scientifically proven solution

demonstration, such as introducing FGD products from serious air pollutants to address all aspects of water, energy, and food nexus, with tangible results at each step.

Acknowledgments

This study acknowledges funding support from the Qatar National Research Fund (QNRF) grant no (NPRP 9-052-2-020). The findings achieved are solely the responsibility of the authors. Open Access funding is provided by the Qatar National Library (QNL). SEM images were accomplished in the Central Laboratories unit, Qatar University.

References

[1] P. Córdoba, Status of flue gas desulphurisation (FGD) systems from coal-fired power plants: Overview of the physic-chemical control processes of wet limestone FGDs, Fuel, 144 (2015) 274-286.

[2] K.P. Resnik, J.T. Yeh, H.W. Pennline, Aqua ammonia process for simultaneous removal of CO_2, SO_2 and NO_x, Int. J. Environ. Technol. Manag., 4 (2004) 89-104.

[3] Y. Jia, Q. Zhong, X. Fan, X. Wang, Kinetics of oxidation of total sulfite in the ammonia-based wet flue gas desulfurization process, Chem. Eng. J., 164 (2010) 132-138.

[4] R.K. Srivastava, W. Jozewicz, Flue gas desulfurization: The state of the art, J Air Waste Manag Assoc., 51 (2001) 1676-1688.

[5] H.N. Soud, Developments in FGD, (2000).

[6] C.R. McLarnon, J.L. Duncan, Testing of ammonia based CO_2 capture with multi-pollutant control technology, Energy Procedia, 1 (2009) 1027-1034.

[7] R.K. Srivastava, Controlling SO_2 emissions--a review of technologies, (2000).

[8] K.P. Resnik, H.W. Pennline, Study of an ammonia-based wet scrubbing process in a continuous flow system, Fuel, 105 (2013) 184-191.

[9] F. Artioli, M. Acuto, J. McArthur, The water-energy-food nexus: An integration agenda and implications for urban governance, Polit. Geogr., 61 (2017) 215-223.

[10] R. Mohtar, R.G. Lawford, J.A. Engel-Cox, Achieving water-energy-food nexus sustainability: A science and data need or a need for integrated public policy?, Front. Environ. Sci., 8 (2020) 132.

[11] C. Ramirez, Y. Almulla, F.F. Nerini, Reusing wastewater for agricultural irrigation: A water-energy-food nexus assessment in the north western sahara aquifer system, Environ. Res. Lett., 16 (2021) 044052.
[12] J.O. Botai, C.M. Botai, K.P. Ncongwane, S. Mpandeli, L. Nhamo, M. Masinde, A.M. Adeola, M.G. Mengistu, H. Tazvinga, M.D. Murambadoro, A review of the water–energy–food nexus research in Africa, Sustainability, 13 (2021) 1762.
[13] H.E. Megerle, S. Niragira, The challenge of food security and the water-energy-food nexus: Burundi case study, in: Hidden hunger and the transformation of food systems, Karger Publishers, **2020**, pp. 183-192.
[14] A.M. Urbinatti, M. Dalla Fontana, A. Stirling, L.L. Giatti, 'Opening up'the governance of water-energy-food nexus: Towards a science-policy-society interface based on hybridity and humility, Sci. Total Environ., (2020) 140945.
[15] M.T. Kashifi, F.S.M. Al-Ismail, S. Chowdhury, H.M. Baaqeel, M. Shafiullah, S.P. Tiwari, S.M. Rahman, Water-energy-food nexus approach to assess crop trading in Saudi Arabia, Sustainability, 14 (2022) 3494.
[16] K. Huang, L. Dai, L. Yu, Y. Fan, G. Huang, Y. Xiao, Q. Wu, Planning regional-scale water-energy-food nexus system management under uncertainty: An inexact fractional programming method, J. Contam. Hydrol., 247 (2022) 103985.
[17] G.-F. Sargentis, P. Siamparina, G.-K. Sakki, A. Efstratiadis, M. Chiotinis, D. Koutsoyiannis, Agricultural land or photovoltaic parks? The water–energy–food nexus and land development perspectives in the thessaly plain, Greece, Sustainability, 13 (2021) 8935.
[18] T. van Gevelt, The water–energy–food nexus: Bridging the science–policy divide, Curr. Opin. Environ. Sci. Health, 13 (2020) 6-10.
[19] B.E. Logan, L. Shi, R. Rossi, Enabling the use of seawater for hydrogen gas production in water electrolyzers, Joule, 5 (2021) 760-762.
[20] S.S. Veroneau, D.G. Nocera, Continuous electrochemical water splitting from natural water sources via forward osmosis, Proc. Natl. Acad. Sci. U. S. A., 118 (2021).
[21] R.T. Porter, M. Fairweather, M. Pourkashanian, R.M. Woolley, The range and level of impurities in CO_2 streams from different carbon capture sources, Int. J. Greenh. Gas Control, 36 (2015) 161-174.

[22] S. Phuntsho, H. Park, D.S. Han, H.K. Shon, Sulfur-containing air pollutants as draw solution for fertilizer drawn forward osmosis desalination process for irrigation use, Desalination, 424 (2017) 1-9.
[23] Y. Cai, W. Shen, J. Wei, T.H. Chong, R. Wang, W.B. Krantz, A.G. Fane, X. Hu, Energy-efficient desalination by forward osmosis using responsive ionic liquid draw solutes, Environ. Sci. Water Res. Technol., 1 (2015) 341-347.
[24] S. Zou, H. Yuan, A. Childress, Z. He, Energy consumption by recirculation: A missing parameter when evaluating forward osmosis, Environ. Sci. Technol., 50 (2016) 6827-6829.
[25] Z. Liu, H. Bai, J. Lee, D.D. Sun, A low-energy forward osmosis process to produce drinking water, Energy Environ. Sci., 4 (2011) 2582-2585.
[26] U. Kang, K.J. Park, D.S. Han, Y.-M. Kim, S. Kim, H. Park, Photoelectrochemical hydrogen production using CdS nanoparticles photodeposited onto Li-ion-inserted titania nanotube arrays, Catal. Today, 303 (2018) 289-295.
[27] H.W. Jeong, K.J. Park, D.S. Han, H. Park, High efficiency solar chemical conversion using electrochemically disordered titania nanotube arrays transplanted onto transparent conductive oxide electrodes, Appl. Catal. B: Environ., 226 (2018) 194-201.
[28] X. Hu, L. Chen, Y. Zhang, Q. Hu, J. Yang, Y. Chen, Large-scale flexible and highly conductive carbon transparent electrodes via roll-to-roll process and its high performance lab-scale indium tin oxide-free polymer solar cells, Chem. Mater., 26 (2014) 6293-6302.
[29] G.S. Gund, D.P. Dubal, S.S. Shinde, C.D. Lokhande, Architectured morphologies of chemically prepared NiO/MWCNTs nanohybrid thin films for high performance supercapacitors, ACS Appl. Mater. Interfaces , 6 (2014) 3176-3188.
[30] H.W. Jeong, K.J. Park, Y. Park, D.S. Han, H. Park, Exploring the photoelectrocatalytic behavior of free-standing TiO_2 nanotube arrays on transparent conductive oxide electrodes: Irradiation direction vs. Alignment direction, Catal. Today, 335 (2019) 319-325.
[31] C. Xiang, L. Sun, Y. Wang, G. Wang, X. Zhao, S. Zhang, Large-scale, uniform, and superhydrophobic titania nanotubes at the inner surface of 1000 mm long titanium tubes, J. Phys. Chem. C, 121 (2017) 15448-15455.
[32] K. Reilly, B. Fang, F. Taghipour, D.P. Wilkinson, Simple and scalable synthesis of vertically aligned anatase nanowires for enhanced photoelectrochemical performance, ACS Appl. Energy Mater., 3 (2020) 8317-8329.

[33] H. Yang, E. Kim, S.H. Kim, M.S. Jeong, H. Shin, Hole trap, charge transfer and photoelectrochemical water oxidation in thickness-controlled TiO_2 anatase thin films, Appl. Surf. Sci, 529 (2020) 147020.
[34] P.M. Pardeshi, A.A. Mungray, Photo-polymerization as a new approach to fabricate the active layer of forward osmosis membrane, Sci. Rep., 9 (2019) 1-13.
[35] A. Tiraferri, Y. Kang, E.P. Giannelis, M. Elimelech, Superhydrophilic thin-film composite forward osmosis membranes for organic fouling control: Fouling behavior and antifouling mechanisms, Environ. Sci. Technol., 46 (2012) 11135-11144.
[36] D.J. Johnson, W.A. Suwaileh, A.W. Mohammed, N. Hilal, Osmotic's potential: An overview of draw solutes for forward osmosis, Desalination, 434 (2018) 100-120.
[37] G.T. Gray, J.R. McCutcheon, M. Elimelech, Internal concentration polarization in forward osmosis: Role of membrane orientation, Desalination, 197 (2006) 1-8.
[38] S. Zou, M. Qin, Z. He, Tackle reverse solute flux in forward osmosis towards sustainable water recovery: Reduction and perspectives, Water Res., 149 (2019) 362-374.
[39] F.-J. Zhao, M. Tausz, L.J. De Kok, Role of sulfur for plant production in agricultural and natural ecosystems, in: Sulfur metabolism in phototrophic organisms, Springer, **2008**, pp. 417-435.
[40] B. Dong, D. Zhu, Q. Yao, H. Tang, X. Ding, Hydrogen-rich water treatment maintains the quality of rosa sterilis fruit by regulating antioxidant capacity and energy metabolism, LWT, 161 (2022) 113361.
[41] W. Cui, P. Fang, K. Zhu, Y. Mao, C. Gao, Y. Xie, J. Wang, W. Shen, Hydrogen-rich water confers plant tolerance to mercury toxicity in alfalfa seedlings, Ecotoxicol. Environ. Saf., 105 (2014) 103-111.